J. Fluid Mech. (2012), *vol.* 708, *pp.* 349–376.
doi:10.1017/jfm.2012.314

Bifurcating flows of plunging aerofoils at high Strouhal numbers

D. J. Cleaver, Z. Wang and I. Gursul†

Department of Mechanical Engineering, University of Bath, Bath BA2 7AY, UK

(Received 22 September 2011; revised 22 March 2012; accepted 19 June 2012;
first published online 8 August 2012)

Force and particle image velocimetry measurements were conducted on a NACA 0012 aerofoil undergoing small-amplitude high-frequency plunging oscillation at low Reynolds numbers and angles of attack in the range 0–20°. For angles of attack less than or equal to the stall angle, at high Strouhal numbers, significant bifurcations are observed in the time-averaged lift coefficient resulting in two lift-coefficient branches. The upper branch is associated with an upwards deflected jet, and the lower branch is associated with a downwards deflected jet. These branches are stable and highly repeatable, and are achieved by increasing or decreasing the frequency in the experiments. Increasing frequency refers to starting from stationary and increasing the frequency very slowly (while waiting for the flow to reach an asymptotic state after each change in frequency); decreasing frequency refers to impulsively starting at the maximum frequency and decreasing the frequency very slowly. For the latter case, angle of attack, starting position and initial acceleration rate are also parameters in determining which branch is selected. The bifurcation behaviour is closely related to the properties of the trailing-edge vortices. The bifurcation was therefore not observed for very small plunge amplitudes or frequencies due to insufficient trailing-edge vortex strength, nor at larger angles of attack due to greater asymmetry in the strength of the trailing-edge vortices, which creates a preference for a downward deflected jet. Vortex strength and asymmetry parameters are derived from the circulation measurements. It is shown that the most appropriate strength parameter in determining the onset of deflected jets is the circulation normalized by the plunge velocity.

Key words: bifurcation, vortex interaction, vortex streets

1. Introduction

Birds, insects, and fish use oscillating wings for lift and thrust production. Their astonishing performance and agility have sparked extensive studies of the flow physics of oscillating wings. Aspects of the unsteady aerodynamics of oscillating aerofoils and wings and vortex-dominated flows have been reviewed by Shyy, Berg & Ljungqvist (1999), Triantafyllou, Triantafyllou & Yue (2000), Ho *et al.* (2003) and Platzer *et al.* (2008). There is growing interest in biologically inspired flows due to their relevance in the design of micro air vehicles (MAVs) and small unmanned underwater vehicles.

† Email address for correspondence: ensiag@bath.ac.uk

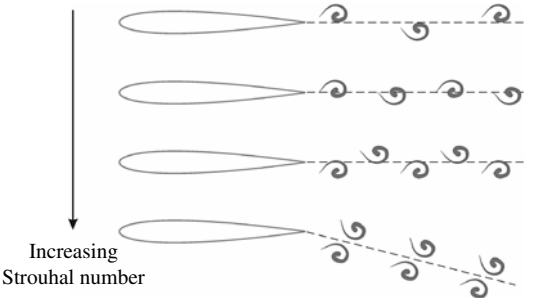

FIGURE 1. Wake patterns with increasing Strouhal number.

1.1. *Lift generation*

For MAVs to become a practical reality it will first be necessary to overcome the limitations of the low-Reynolds-number aerodynamics. Natural flyers have managed to circumvent this barrier through the exploitation of unsteady aerodynamic phenomena, for example the leading-edge vortex (LEV), clap and fling, etc. Of these, the LEV is generally accepted (Sane 2003) as being responsible for the majority of lift augmentation. The LEV is produced during the wing's downstroke and once formed it convects over the upper surface creating a low-pressure wave as it passes. The behaviour of the LEV once shed will largely be determined by the Strouhal number based on the chord length, which can be considered as the ratio of two time scales:

$$St_c = f\,c/U_\infty, \tag{1.1}$$

where f is the oscillation frequency, c the aerofoil chord, and U_∞ the free-stream velocity. Hence it is expected that the Strouhal number based on the chord length will be important in determining the unsteady lift.

To produce the LEV, natural flyers use a large-amplitude low-frequency flapping motion, hence low St_c, of $O(0.1)$. However, the opposite approach, which is the small-amplitude high-frequency (large-St_c) motion, has also been considered for MAV applications (Cleaver, Wang & Gursul 2009*a*,*b*, 2010, 2011). A lift-enhancing LEV is still generated by small-amplitude high-frequency motion, which is more appropriate for electrical actuators, and also preferable as a stable sensor platform. This approach is also more suitable for exploitation of the aeroelastic vibrations for flow control purposes, through excitation of the frequencies of the dominant inherent instabilities of the separated flows by wing oscillations. It has been shown (Cleaver *et al.* 2011) that when the excitation frequency corresponds to that of the wake instabilities ($St_c = O(1)$), optimal conditions are reached for lift generation. Fortunately, these frequencies are of the same order of magnitude as the structural frequencies of small vehicles.

1.2. *Thrust generation*

Thrust generation with oscillating (plunging, pitching) aerofoils or oscillating free stream was discussed nearly one hundred years ago. The history of the subject is given in the review article by Platzer *et al.* (2008). At low Strouhal numbers the vortices are spaced symmetrically about the horizontal plane, with the clockwise vortex above the counter-clockwise one creating a wake similar to a Kármán vortex street, see figure 1. This is considered drag indicative due to the time-averaged velocity deficit in the wake. With increasing Strouhal number these vortices gradually become inverted creating a

reverse Kármán vortex street. (Although it was shown recently that the switch in the vortex array orientation does not exactly coincide with the switch from drag to thrust (Godoy-Diana, Aider & Wesfreid 2008; Bohl & Koochesfahani 2009), this picture gives an approximate tool to discuss the state of the flow.) Once the reverse Kármán vortex street is observed, due to the time-averaged velocity surplus in the wake this is generally considered indicative of thrust production. Up to this point, if the aerofoil were to be oscillated at zero angle of attack, one would anticipate symmetry about the horizontal plane and therefore zero time-averaged lift.

It has been shown that the most important parameter for thrust generation is the Strouhal number based on the amplitude, which is defined as

$$St_A = f A / U_\infty, \tag{1.2}$$

where A is the peak-to-peak amplitude of the trailing edge. This parameter can also be considered as normalized plunge velocity. It is related to the maximum effective angle of attack $\alpha_{eff,max}$, through

$$\alpha_{eff,max} = \alpha + \tan^{-1}\frac{U_P}{U_\infty} = \alpha + \tan^{-1}\frac{2\pi f a}{U_\infty} = \alpha + \tan^{-1}\pi\, St_A \tag{1.3}$$

where U_P is the maximum plunge velocity. Hence, with increasing St_A, the effective angle of attack increases, and flow separation from the leading edge and leading-edge vortex formation take place. The leading-edge vortices are omitted from the flow schematic in figure 1.

1.3. *Deflected jets*

For zero mean angle of attack, the symmetry may be broken by deflected jets with increasing Strouhal number. Figure 1 shows the transition towards symmetry breaking. Thus at high enough Strouhal numbers there is the possibility of asymmetric flow fields and non-zero lift even at zero angle of attack. As we will demonstrate, higher time-averaged lift can be generated in this mode compared to the flow field without deflected jets. Hence, this is another motivation to investigate small-amplitude high-frequency motion.

According to Jones, Dohring & Platzer (1998) such deflected jets were first observed by Bratt (1950) but not commented on. In their own experiments Jones *et al.* (1998) observed deflected jets when $St_A > 0.32$. The vortex streets could be deflected up or down, hence they were termed *dual* modes. It was also observed that small disturbances could trigger the switch between the modes in a random fashion. Jones *et al.* (1998) were also able to simulate such deflected jets by an inviscid unsteady panel code; however, the jets were very stable and did not exhibit any switch. In the simulations, the direction of the deflection was determined by the sign of the starting vortex when the aerofoil starts to move up or down. In viscous simulations, Lewin & Haj-Hariri (2003) observed aperiodic and asymmetric solutions, corresponding to unstable deflected jets for an aerofoil oscillating at $St_A \approx 0.48$ and at Reynolds number $Re = U_\infty c/\nu = 500$ (where ν is the kinematic viscosity). Heathcote & Gursul (2007*b*) experimentally observed jet switching for aerofoils oscillated in still fluid. The jet switching was observed to be periodic with a period two orders of magnitude larger than the plunging period ($O(100T)$). Recently, von Ellenrieder & Pothos (2008) observed stable deflected jets to commence when $St_A > 0.43$ for a NACA 0012 aerofoil plunging at $a/c = 0.215$ for $Re = 2700$. The direction, upwards or downwards, was established when the heaving motion was initiated and remains the same as long as the motion is continued. Liang *et al.* (2011) were able to

reproduce the experimental results of Jones *et al.* (1998) and predicted that the degree of asymmetry increases with Reynolds number in the range of $Re = 252$–1850.

For pitching aerofoils, such deflected jets have been computationally simulated (Emblemsvag, Suzuki & Candler 2002). For a Reynolds number of $Re = 200$, asymmetric flow was predicted for $St_A = 0.42$. Furthermore, deflected jets have also been observed experimentally for pitching aerofoils (Godoy-Diana *et al.* 2008, 2009) with onset around $St_A \approx 0.33$–0.44 for $Re = 255$. It was also conjectured (Godoy-Diana *et al.* 2008) that, as natural flyers typically operate in the range $0.2 < St_A < 0.4$, animals using flapping-based propulsion could exploit deflected jets for manoeuvring. Indeed, Wang (2000) identified downward deflected vortex dipoles as a possible method of lift generation in hovering insect flight.

Given the potential for large force coefficients, the prediction of the onset conditions for this asymmetry or bifurcation may be very useful for MAV design and control. Emblemsvag *et al.* (2002) were the first to suggest that, at high frequencies, the vortices tend to shed in pairs (vortex dipoles) and this triggers the deflected wakes. Hence, the formation of dipoles is important as the distance between the vortices decreases and strength of the vortices increases with increasing frequency. A symmetry-breaking criterion, based on a simple model of a dipole and its self-induced velocity, was suggested by Godoy-Diana *et al.* (2009). The model was developed based on the measured strength of the vortices and the phase velocity of the vortex street for zero mean angle of attack.

1.4. *Objectives*

Previous studies have focused on the formation of deflected jets when the mean angle of attack was zero. These observations led to symmetry breaking and bifurcation at high Strouhal numbers. However, the geometric symmetry is removed when the mean angle of attack is non-zero. Hence a second parameter, which is the angle of attack and defines the degree of asymmetry, is introduced in this study. Whether the bifurcations are still observed and, if observed, the range of incidences over which they occur will be investigated by means of flow field and force measurements. From a practical point of view, the non-zero mean incidence is more meaningful.

To the best of our knowledge no previous study has experimentally measured the effect of deflected jets on the time-averaged force coefficients, nor how the initial conditions determine the direction of the deflected jet. Starting with the stationary aerofoil, we measure the time-averaged lift as we increase the frequency very slowly up to a maximum value, and stop the motion. Then we restart the motion impulsively at the maximum frequency and decrease the frequency very slowly. Before each measurement we wait for the flow to reach an asymptotic and stable state. Following this procedure, we identify the bifurcation points for each angle of attack.

The remainder of the paper is as follows. Section 2 explains the experimental set-up, and the methods used for force and velocity measurements. Section 3 presents the bifurcation behaviour at different angles of attack using the time-averaged lift measurements and corresponding flow fields. Effects of initial conditions, oscillation amplitude and Reynolds number are investigated. Also, in this section, various bifurcation criteria are developed and discussed. Section 4 contains the conclusions.

2. Experimental methodology

Force and particle image velocimetry (PIV) measurements were conducted on a plunging NACA 0012 aerofoil mounted vertically in a closed-loop water tunnel. The

aerofoil was maintained at a fixed geometric angle of attack with the sinusoidal plunging motion acting normal to the free stream. The experiments presented here are for a Reynolds number based on the chord length of $Re = 10\,000$.

2.1. *Experimental setup*

The experiments were conducted in a free-surface closed-loop water tunnel (Eidetics Model 1520) at the University of Bath. The water tunnel is capable of flow speeds in the range 0–0.5 m s^{-1} and has a working section of dimensions 381 mm × 508 mm × 1530 mm. The turbulence intensity has previously been measured (Heathcote & Gursul 2007*a*) by laser Doppler velocimetry to be less than 0.5 %.

A NACA 0012 aerofoil of dimensions 0.1 m chord × 0.3 m span was mounted vertically in a 'shaker' mechanism, see figure 2. The aerofoil was constructed by rapid prototyping from SLS Duraform Prototype PA, and had two internal 8 mm diameter steel rods spanning from root to tip to ensure a high spanwise stiffness. The tip deformation was monitored with a digital camera and did not exceed 1 % of the chord length for the largest amplitude and frequency. The aerofoil was placed between an upper and lower end plate with clearances maintained at 2 mm. The oscillations were supplied via a Motavario 0.37 kW three-phase motor, 5:1 wormgear and IMO Jaguar controller. The position of the root of the aerofoil was measured through a rotary encoder attached to the spindle of the wormgear shaft. The rotary encoder was also used to trigger the PIV system.

We consider harmonic plunge oscillations in the form

$$h = a \cos 2\pi f t. \tag{2.1}$$

The normalized amplitude of the plunge oscillations was in the range of $a/c = 0.025$–0.2. The Strouhal number based on the chord length, $St_c = f c/U_\infty$, was varied in the range of $St_c = 0$–3.0, with a maximum uncertainty of ±2.3 %. Uncertainties are calculated based on the methods of Moffat (1988) taking into account both bias and precision errors.

2.2. *Force measurements*

The forces applied in both the streamwise and cross-stream directions were measured via a two-component binocular strain-gauge force balance (Frampton *et al.* 2002). The measured forces include both time-dependent aerodynamic forces and the inertia force in the cross-stream direction. However, as the time-averaged inertial force over a complete cycle is zero, the time-averaged forces include only the time-averaged aerodynamic component. No attempt was made to estimate the instantaneous aerodynamic forces, as the time-averaged aerodynamic forces are sufficient for the current study.

Three force balances, two aluminium and one mild steel, of varying sensitivity (hence flexibility) were used as the oscillation frequency is increased. A fourth very sensitive aluminium force balance was used for the stationary measurements. Within their applicable ranges, the agreement between the three balances was excellent. The signal from the strain gauges was amplified by a Wheatstone bridge circuit and sampled at either 2 kHz for 20 000 samples (stationary cases), or 360 samples per cycle for a minimum of 50 cycles (dynamic cases). To minimize uncertainty the calibration curves consisted of 23 points, and calibration was performed daily before and after testing. Each data set was repeated a minimum of three times for each force balance.

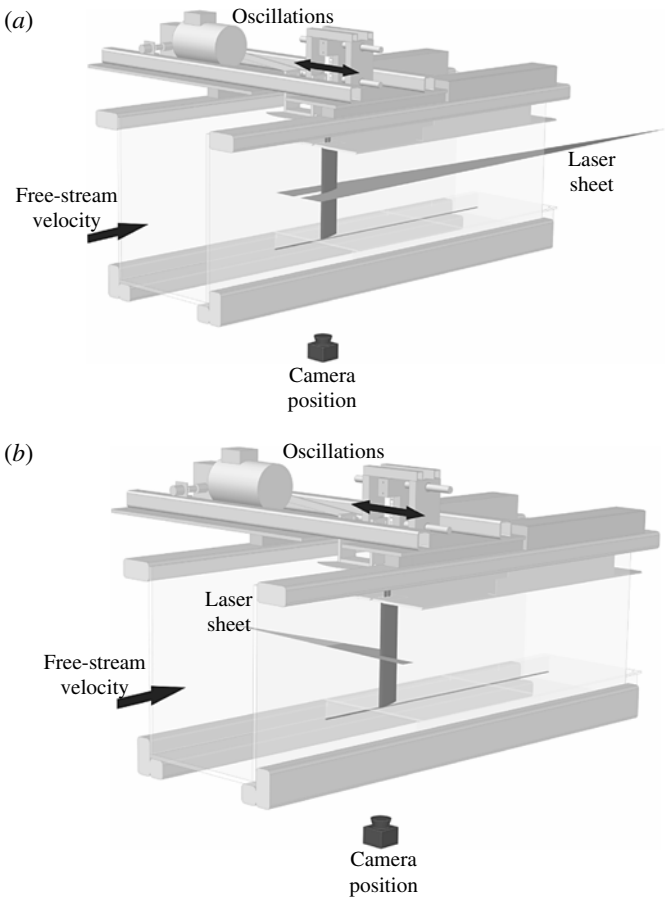

FIGURE 2. Experimental setup: (*a*) for PIV measurements over the upper surface; and (*b*) for PIV measurements over the lower surface.

The uncertainty associated with these time-averaged force measurements increases with increasing frequency. For a typical case the uncertainty of the time-averaged lift coefficient increases from ± 0.03 at $St_c = 0$, to ± 0.35 at the maximum Strouhal number. Likewise the uncertainty of the time-averaged drag coefficient increases from ± 0.02 to ± 0.09 within the same range.

2.3. *PIV measurements*

A TSI 2D-PIV system consisting of dual 50 mJ Nd:YAG lasers and an 8-bit CCD camera of resolution 1600 by 1192 pixels was used to measure the velocity field in the vicinity of the aerofoil. The flow was seeded with commercially available hollow glass particles with mean diameter of 4 μm. For measurements over the upper surface of the aerofoil, the laser sheet was positioned at mid-span, with the camera located under the tunnel as shown in figure 2(*a*). The shadow created by the aerofoil therefore obscured the lower surface. For measurements over the lower surface the laser sheet was positioned near the sidewall of the tunnel as shown in figure 2(*b*). The PIV images were analysed using the software Insight 3G using a recursive FFT correlator with a final interrogation window size of 16 by 16 pixels to generate a vector field

of 199 × 148 vectors. This gave approximately a 1.2 mm (1.2 % of the chord length) spatial resolution for the upper surface, and 0.9 mm (0.9 % of the chord length) for the lower surface. The estimated uncertainty for velocity measurements is 2 % of the free-stream velocity U_∞. The time-averaged data are derived from 500 pairs of images, the phase-averaged from 100 pairs for the upper surface, and between 100 and 250 pairs for the lower surface. Where necessary the upper and lower surface data were later merged through interpolation of the upper surface data onto the lower surface grid.

To calculate circulation from the phase-averaged data, the vortex is located using a vortex identification algorithm (Graftieaux, Michard & Grosjean 2001; Morgan, Babinsky & Harvey 2009) with the search centred on the point of maximum absolute vorticity. The radius of the vortex is then determined by continually expanding from the centre, one spatial resolution unit at a time, until the increase in the magnitude of circulation is negative or small (<1 %). The circulation calculation itself is done using both line integral and vorticity surface methods (Godoy-Diana *et al.* 2009). The agreement between the two methods was generally very good. All circulation results presented herein are derived from the average of the two.

3. Results and discussion

3.1. *Stationary aerofoil*

The experiments for the plunging aerofoil were carried out for a Reynolds number of $Re = 10\,000$. As a reference case, the lift force measurements and the time-averaged velocity measurements for the stationary two-dimensional NACA 0012 aerofoil are presented in Cleaver *et al.* (2010). Based on these measurements, the stall angle is $\alpha_S = 10^\circ$ for this Reynolds number. The angles of attack under consideration in this paper can therefore be classified as: $\alpha = 0$ and 5° is pre-stall, $\alpha = 10^\circ$ is stall, and $\alpha \geqslant 12.5^\circ$ is fully stalled.

3.2. *Bifurcations*

Shown in figure 3 is the time-averaged lift coefficient for a NACA 0012 aerofoil oscillating at an amplitude of $a/c = 0.15$, and six different angles of attack. A solid line represents data collected by starting at $St_c = 0$ (stationary), and then increasing the frequency in steps, recording data at each point. A dashed line represents data collected by impulsively starting at the maximum Strouhal number, and then decreasing the frequency in steps, recording data at each point. After each change in frequency, we waited for sufficient settling time and then measured the time-averaged forces. Then we moved to a new frequency and repeated the procedure. Hence there are no transient force data. Even when the aerofoil motion is started impulsively at the high frequency we waited for the flow to reach an asymptotic state, and then measured the time-averaged force.

For $\alpha = 0^\circ$ there are three curves: one for increasing frequency, and two for decreasing frequency, where the two starting positions of the aerofoil are $h_i = +a$ (solid symbol, dashed line) and $h_i = -a$ (open symbol, dashed line). These curves were highly repeatable when the experiments were carried out on different occasions. Up to $St_c = 1.5$ all three match closely. They all begin at $c_l = 0$ and continue along $c_l = 0$ until $St_c > 1.25$ where all three become slightly positive suggesting a slight asymmetry developing. After $St_c = 1.5$ the three curves diverge significantly producing two distinct results: increasing and decreasing ($h_i = a$) frequency produce very large positive lift coefficients; decreasing ($h_i = -a$) frequency produces very large negative

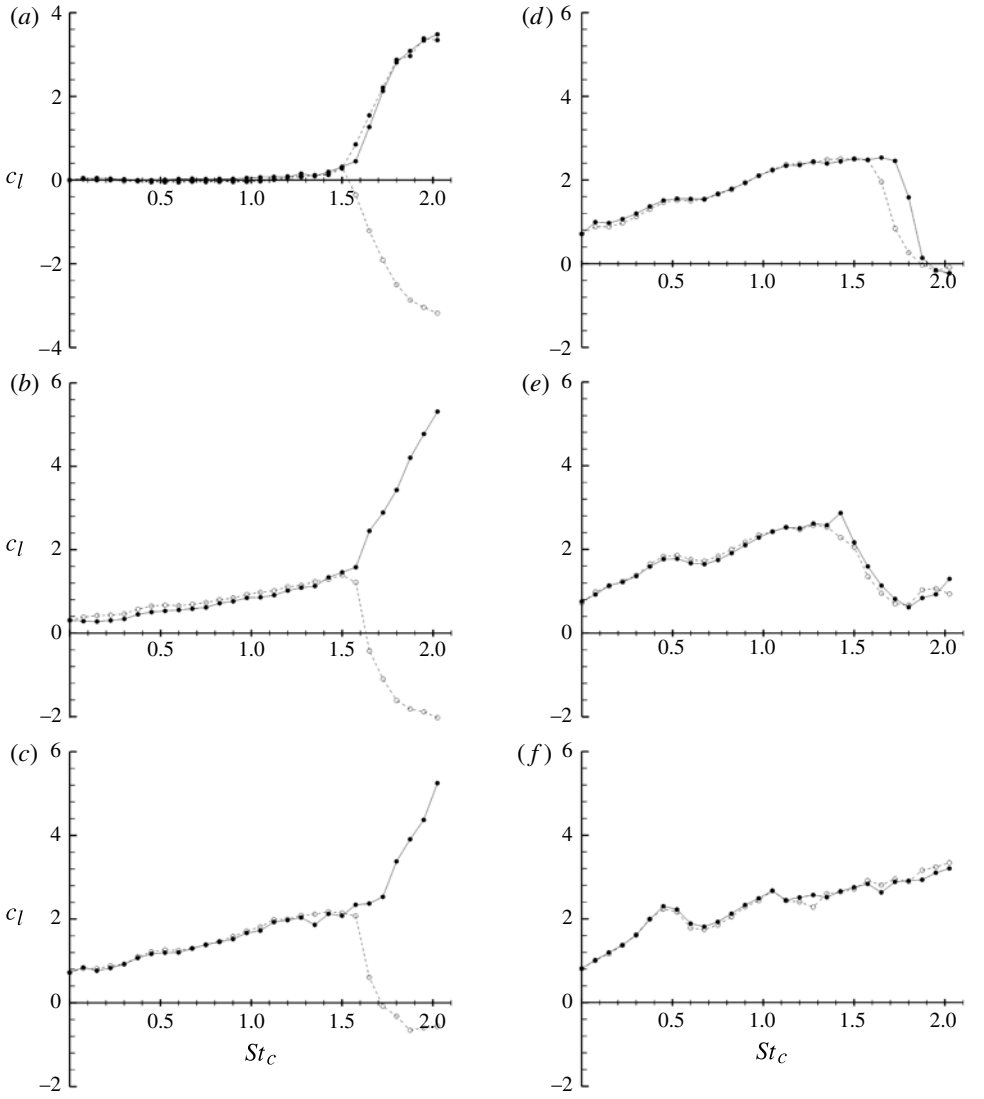

FIGURE 3. Time-averaged lift coefficient for $a/c = 0.15$ and all angles of attack considered. Solid line represents increasing frequency, dashed line represents decreasing frequency with a starting position for $\alpha = 0°$ of $h_i = \pm a$, and for $\alpha > 0°$ $h_i = 0$ (aerofoil moving upwards): (*a*) $\alpha = 0°$; (*b*) $\alpha = 5°$; (*c*) $\alpha = 10°$; (*d*) $\alpha = 12.5°$; (*e*) $\alpha = 15°$; (*f*) $\alpha = 20°$.

lift coefficients. Hence for the same experimental conditions two entirely different results are possible; indeed the two results are approximately mirror images of each other in the *x*-axis. Which branch is selected is determined by the initial conditions (increasing/decreasing frequency, starting position, etc.), but the branch is unaffected by the initial conditions (note the similarity of the upper branch for increasing and decreasing frequency). Hereafter where two distinct results exist for the same experimental conditions it will be termed a dual flow, with the positive-lift-coefficient branch termed *mode A* and the negative branch termed *mode B*.

With the angle of attack increased to $\alpha = 5^\circ$ there are similarly two distinct results determined by the initial conditions. Increasing frequency results in mode A, and decreasing frequency results in mode B. For decreasing frequency the effect of starting position will be considered in more detail later, but it suffices to say that given a suitable h_i either mode can be produced. For conciseness only a single starting position that produces mode B is considered here, i.e. $h_i = 0$ (moving upwards). The principal difference at this angle of attack is the lack of symmetry. Mode A therefore results in a maximum lift coefficient of $c_l = 5.3$, and mode B a minimum of $c_l = -2.0$. With the angle of attack increase to $\alpha = 10^\circ$ this asymmetry is enhanced resulting in a maximum lift coefficient of $c_l = 4.3$ and minimum of $c_l = -0.4$.

At $\alpha = 12.5^\circ$ there are no longer two distinct results at the highest Strouhal number, instead both increasing and decreasing frequency result in a slightly negative lift coefficient. In the low-Strouhal-number range the match is very close. At $St_c = 1.63$ increasing and decreasing frequency diverge slightly, remerging at $St_c = 1.88$. The behaviour in this range can be considered as a hysteresis loop.

At $\alpha = 15^\circ$ there is similar behaviour to $\alpha = 12.5^\circ$ except the hysteresis is reduced and the fall in lift does not result in a negative lift coefficient. The features associated with this post-stall angle of attack and enhanced time-averaged lift were discussed in detail by Cleaver *et al.* (2011). The peaks were attributed to resonance with the natural wake shedding frequency, its harmonics or subharmonics. The fall in lift at $St_c \approx 1.5$ was attributed to the disintegration of the upper-surface LEV (due to a strong vortex–aerofoil interaction) combined with the growth of a lower-surface LEV.

With the angle of attack increased to $\alpha = 20^\circ$ there is no longer a fall in lift at $St_c \approx 1.5$; instead there is a continued increase in lift coefficient with Strouhal number. Superimposed onto this are several peaks which can be attributed to resonance with the natural wake shedding frequency as for $\alpha = 15^\circ$. The crucial point is that both increasing and decreasing frequency curves match, and there is no hysteresis and bifurcation.

In summary, for angles of attack up to the stall angle, $\alpha \leqslant 10^\circ$, dual flows are possible resulting in extremely different and potentially very large time-averaged lift coefficients. Which flow field is created is dependent upon the initial conditions. With increasing frequency and $0^\circ < \alpha \leqslant 10^\circ$ only mode A is achievable. With decreasing frequency, either mode may be obtained depending upon the starting position and angle of attack. In the post-stall region, $10^\circ < \alpha < 20^\circ$, except for some minor hysteresis loops, the lift for both increasing and decreasing frequency matches. While the convected LEVs enhance the time-averaged lift in the post-stall region, there is even higher lift due to the bifurcations in the pre-stall region. As will be shown below, the mechanism for high lift is deflected (thrust-producing) jets at high Strouhal numbers.

3.3. *Bifurcation flow fields*

Figures 4 and 5 show PIV measurements for $a/c = 0.15$ and $\alpha = 0^\circ$, demonstrating pre-bifurcation, mode A, and mode B flow fields. In figure 4 these are in the form of time-averaged velocity magnitude. Figure 4(*a*), for a pre-bifurcation flow field, clearly shows a time-averaged jet aligned horizontally. The associated phase-averaged vorticity fields in figure 5 (left column) demonstrate this jet to be the result of a reverse Kármán vortex street. During the downward motion (*a*–*c*) a counter-clockwise vortex forms and sheds from the trailing edge; during the upward motion (*c*–*a*) a clockwise vortex forms and sheds. Both of these vortices convect along a path approximately aligned with the horizontal with equidistant spacing. At the leading

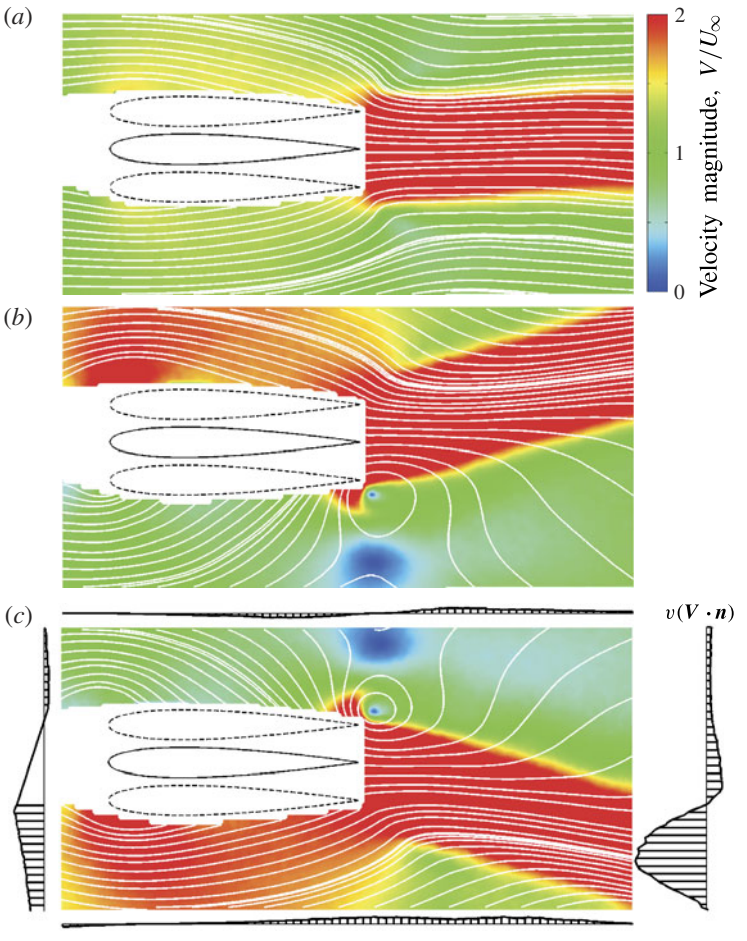

FIGURE 4. (Colour online) Time-averaged velocity magnitude for $a/c = 0.15$, $\alpha = 0°$, and: (*a*) $St_c = 1.500$ – pre-bifurcation; (*b*) $St_c = 2.025$ – mode A; (*c*) $St_c = 2.025$ – mode B. Solid lines show the mean position, dashed lines show the maximum and minimum aerofoil position. For (*c*) arrows show momentum flux component in the vertical direction for the boundaries of the control volume.

edge an upper-surface clockwise vortex forms during the downward motion (see phase *c*) and is dissipated during the upward motion through impingement on the upward-moving aerofoil as previously described by Visbal (2009) and Cleaver *et al.* (2011). Conversely, during the upward motion a counter-clockwise leading-edge vortex forms (see phase *a*) which is dissipated during the downward motion. The flow field as a whole is characterized by symmetry about the horizontal plane justifying the near-zero time-averaged lift coefficient.

With the Strouhal number increased into the dual-flow regime this symmetry is broken, see figure 4(*b,c*). For mode A the time-averaged jet is deflected upwards and there is a high-velocity region over the upper surface. For mode B the inverse is true: a downwards deflected jet and a high-velocity leading-edge region over the lower surface. The phase-averaged vorticity shown in figure 5 identifies the cause to be trailing-edge vortex dipole formation. For mode A (centre column) a clockwise

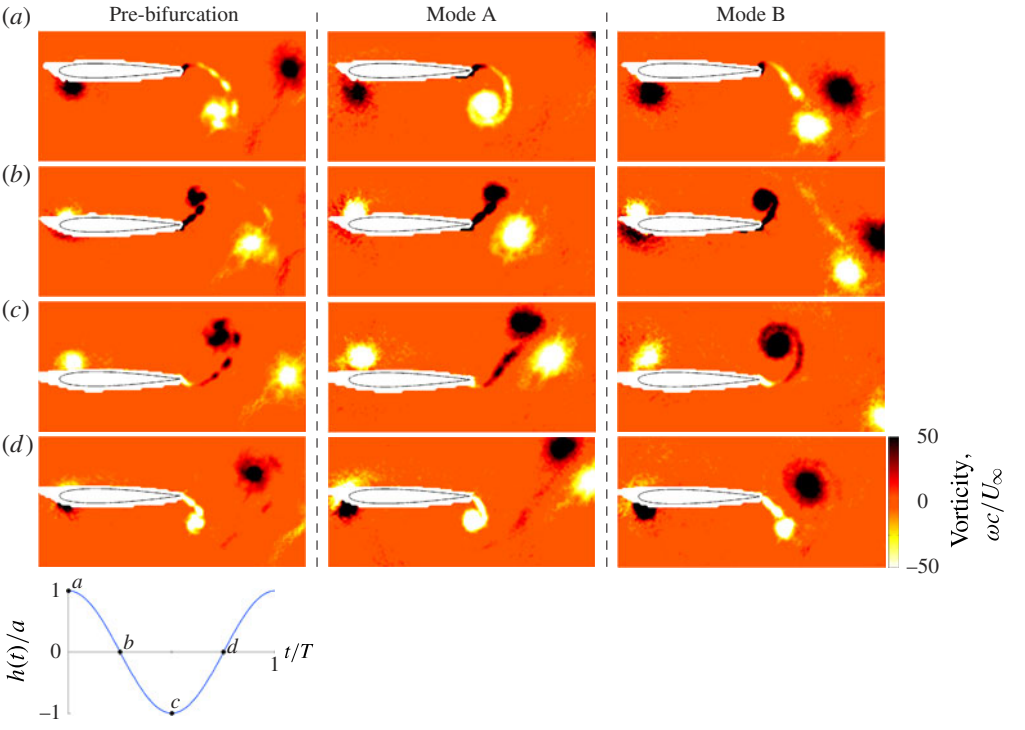

FIGURE 5. (Colour online) Phase-averaged vorticity contour plots for the same cases as in figure 4. The points in the cycle are shown on the diagram at the bottom.

trailing-edge vortex (TEV) forms during the upward motion (*c–a*) and 'loiters' near the aerofoil during the downward motion (*a–c*) during which the counter-clockwise TEV forms. As a result of their proximity the vortices form a dipole that due to the relative positions of the vortices has a self-induced velocity in the upwards direction, thereby creating an upwards deflected jet. For mode B (right column) the inverse is true, i.e. the counter-clockwise TEV loiters, creating a vortex dipole with a downwards self-induced velocity and therefore a downwards deflected jet. The mode-B flow field therefore appears mirrored in the horizontal and 180° out of phase with the mode-A flow field, compare figure 5(*c*) (centre) with figure 5(*a*) (right).

Due to the asymmetry of the flow near the trailing edge, asymmetry is also created near the leading edge. Mode A has a strong upper-surface LEV (figure 5*c* centre), and comparatively weak lower-surface LEV (figure 5*a* centre), explaining both the high time-averaged velocity above the upper surface observed in figure 4(*b*) and also the very high positive time-averaged lift coefficient, $c_l \approx 3.4$. For mode B the inverse is true, i.e. a weak upper-surface LEV and strong lower-surface LEV resulting in a large negative lift coefficient. Hence, the lift direction is the same as the direction of the vertical component of the deflected jet. This is consistent with the simulations performed at much lower Reynolds numbers ($Re = 200$ in Emblemsvag *et al.* 2002; $Re = 1850$ in Liang *et al.* 2011).

Both figures 4 and 5 are for zero angle of attack where symmetry about the horizontal plane simplifies the problem. However, as suggested by the force data shown in figure 3, similar dual flows exist for non-zero angles of attack. Figure 6 therefore shows phase-averaged vorticity contours for mode A and mode B for the

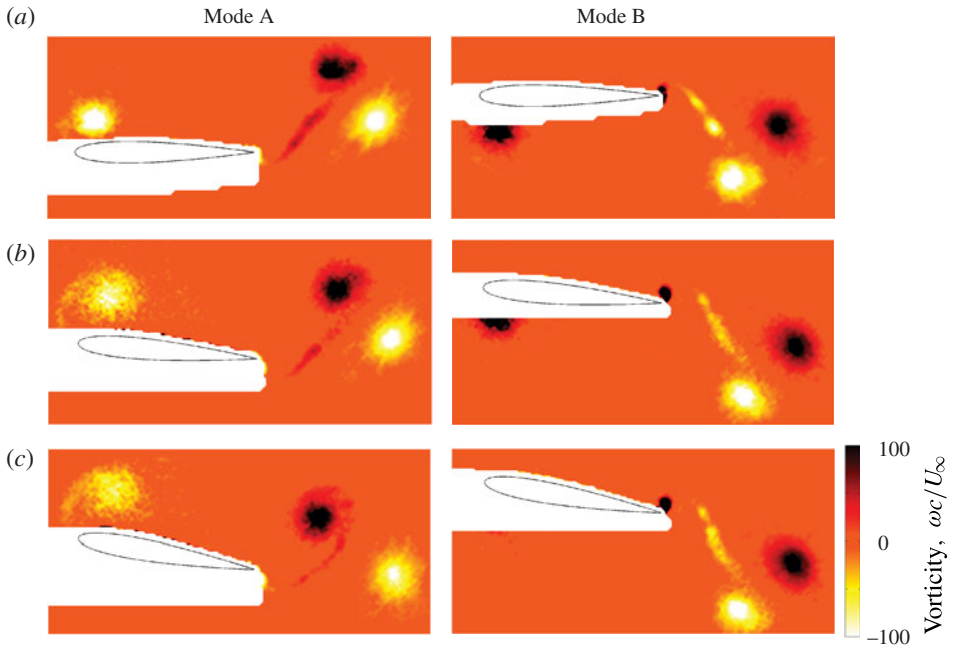

FIGURE 6. (Colour online) Phase-averaged vorticity contour plots comparing the mode-A flow field (left) at the bottom of the motion, and mode-B flow field (right) at the top of the motion for $a/c = 0.15$, $St_c = 2.025$ and: (*a*) $\alpha = 0°$; (*b*) $\alpha = 5°$; (*c*) $\alpha = 10°$.

three angles of attack that exhibit dual flows. For mode A (left column), the aerofoil is at the bottom of its motion. For mode B (right column), the aerofoil is at the top of its motion. Figure 6 shows that qualitatively the wake structure is independent of angle of attack in this range. In all cases there is a TEV dipole, which, due to the vortex positions, convects upwards or downwards. It can therefore be concluded that the same phenomenon, deflected jets, is responsible for the lift force bifurcations observed for $\alpha \leqslant 10°$.

It is interesting to note that an upwards deflected jet (mode A) is associated with high lift for $\alpha \leqslant 10°$ in figure 3 and a downwards deflected jet (mode B) is associated with low (and even negative) lift. This relationship between the direction of the lift and deflected jet is contrary to what one would intuitively expect. To understand why, below is a simple control-volume analysis. It is simple in the sense that it is performed on the time-averaged flow. (The complete analysis would involve the fluctuating velocity-squared-type terms, which we do not have as the PIV measurements in this study are not time-resolved.) The momentum theorem for the control volume in the vertical direction (y-axis) is

$$\int_{HS} \Delta p_{UL}\, \mathrm{d}A - L = \int_{CS} \rho v(\boldsymbol{V}\cdot\boldsymbol{n})\, \mathrm{d}A \tag{3.1}$$

where Δp_{UL} is the pressure difference between the upper and lower boundaries, L is the lift force, $\boldsymbol{V} = u\boldsymbol{i} + v\boldsymbol{j}$, $\boldsymbol{n}$ is the unit normal vector, CS refers to the control surfaces and HS refers to the horizontal (top and bottom) control surfaces. The variation of the momentum flux terms on the right-hand side are calculated for the control surfaces and are sketched at the boundaries of the control volume in figure 4(*c*). The measured

time-averaged lift ($L = -1.80$ N m^{-1}) and the momentum flux terms were substituted into the momentum equation:

$$\int_{HS} \Delta p_{UL}\, \mathrm{d}A - (-1.80 \text{ N m}^{-1}) = -0.315 \text{ N m}^{-1}. \tag{3.2}$$

This equation shows that the momentum flux terms have a small contribution to the lift force. The main contribution comes from the pressure difference between the upper and lower boundaries:

$$\int_{HS} \Delta p_{UL}\, \mathrm{d}A = -2.12 \text{ N m}^{-1}. \tag{3.3}$$

The momentum equation provides an estimate of the contribution of the pressure term, which can be compared with a rough estimate of the pressure calculated by applying the steady Bernoulli equation to the time-averaged velocity at the boundaries. We found that the latter is 1.18 times the former. Considering the level of simplification, this is reasonable. In summary, momentum in the deflected jet makes a small contribution to the lift force, and the lift force is instead dominated by the pressure difference due to the velocity difference over the upper and lower surfaces as observed in figure 4.

3.4. *Effect of initial conditions*

In this section, we study how the initial conditions determine which branch is selected through the use of transient data (instantaneous velocity) rather than the phase-averaged velocity used in previous sections. The initial conditions can be divided into two broad categories: increasing and decreasing frequency. For increasing frequency, the starting position is always the stationary case, and the result is the same, mode A, for all three angles of attack. This is unexpected for $\alpha = 0°$, as symmetry means that logically mode B is equally likely. Although there is a starting vortex when the aerofoil starts its motion from rest, the vortex street remains symmetric until much higher frequencies. Therefore this suggests that the effect of initial asymmetry introduced by the starting vortex is not important for the case of increasing frequency. Practically, however, perfect symmetry is impossible to achieve experimentally, and in practice the mode B case only occurred once in twelve occasions (and is therefore not presented here). From this it can be concluded that for increasing frequency the direction of the deflected jet is extremely susceptible to even slight asymmetry.

For decreasing frequency the situation is more complicated. For $\alpha = 0°$, symmetry means either case is equally possible and it has previously been shown (von Ellenrieder & Pothos 2008) that starting position is the determining factor. This is further complicated because there are an infinite number of possible starting positions in the range $-a \leqslant h_i \leqslant a$, and because experimentally a true impulsive start (meaning an infinite acceleration to full frequency) is not physically possible. For the purposes of this study the acceleration time is measured to be less than the full period as demonstrated in the inset of figure 7, and only the two extreme starting positions are considered in detail: $h_i = a$, and $-a$. The effect of these starting positions on whether mode A or B is produced is shown in table 1. These are derived from ten repeats for each starting position. For all angles of attack and amplitudes, starting with a position of $h_i = -a$ produces mode B (downwards deflected jet). Starting with a position of $h_i = a$ is more complicated. For $\alpha = 0$ and 5° this starting position consistently produces mode A (upwards deflected jet), but at $\alpha = 10°$ it only produces an upwards deflected jet at a single amplitude and only 20 % of the time. In all other

Angle of attack, α		0°	5°	10°		
	a/c	0.15	0.15	0.10	0.15	0.20
Starting position, h_i:	a	A	A	B	B (80 %)	B
	$-a$	B	B	B	B	B

TABLE 1. Effect of starting position on the mode produced.

cases a mode B case is produced. This suggests that the direction of the deflected jet is determined by various parameters, i.e. starting position, angle of attack, and possibly the initial acceleration rate. It is important to note that for $\alpha > 0°$ in figures 3 and 6 a starting position of $h_i = 0$ (up) was used to guarantee a mode-B flow field.

To investigate how starting position and angle of attack influence the direction of the deflected jet, shown in figure 7 are selected instantaneous PIV images from the first two cycles. For $\alpha = 0°$ the first counter-clockwise vortex can be seen as CCW1 in A, and then again at the top of the next cycle next to the first clockwise vortex (CW1) in B. During the course of the next cycle it can be seen that the first counter-clockwise vortex has little effect on the outcome as the first clockwise vortex pairs with the second counter-clockwise vortex instead. As a result the first vortex dipole convects upwards. By contrast for $\alpha = 10°$ the first clockwise vortex pairs with the first counter-clockwise vortex drawing it downwards, see B-F (figure 7*b*). This results in a flow field, where the counter-clockwise TEV loiters and pairs with the clockwise TEV to give a downwards deflected jet. The reason for the increased effect of the first counter-clockwise vortex at $\alpha = 10°$ is its increased strength. This is quantified through the absolute circulation measurements shown in figure 8. For $\alpha = 0°$ (solid lines), there is a very large difference between the circulation of the first counter-clockwise and clockwise TEV. This is due to the aforementioned acceleration time which results in the aerofoil moving slower in the first downwards motion than the first upwards one. For $\alpha = 10°$ the gap in vortex strengths is reduced due to the positive bias in the effective angle of attack. This enables the first clockwise TEV to pair with the first counter-clockwise one and therefore create a downward deflected jet. It is therefore important to note that different acceleration rates could cause different results.

3.5. *Effect of amplitude*

Now we return to the stable branches (bifurcation solutions) and investigate the effect of oscillation amplitude. Again, all time-averaged force and phase-averaged velocity data are taken after the flow has settled following a change in frequency. Shown in figure 9 are the time-averaged lift coefficient for five amplitudes, at four angles of attack $\alpha = 0°$, 5°, $10°$, and $15°$. Figure 9(*a*) shows the data for $\alpha = 0°$; and for each amplitude three initial conditions are considered: increasing frequency, decreasing frequency with $h_i = a$, and decreasing frequency with $h_i = -a$. Neither $a/c = 0.025$ nor 0.050 exhibits bifurcation behaviour. For $a/c \geqslant 0.10$, however, bifurcation behaviour is evident as previously discussed. The Strouhal number of the onset of bifurcation is delayed by smaller amplitude, hence the bifurcation occurs at $St_c = 1.25$, 1.50 and 2.00 for $a/c = 0.20$, 0.15 and 0.10 respectively. Similarly for $\alpha = 5°$ and $10°$ (see figure 9*b,c*), bifurcation only occurs for $a/c \geqslant 0.10$, with increasing frequency becoming mode A and decreasing frequency becoming mode B. Again the point of bifurcation is amplitude dependent but slightly delayed from that for $\alpha = 0°$. The bifurcation points for $\alpha = 5°$ are therefore $St_c = 1.30$, 1.58

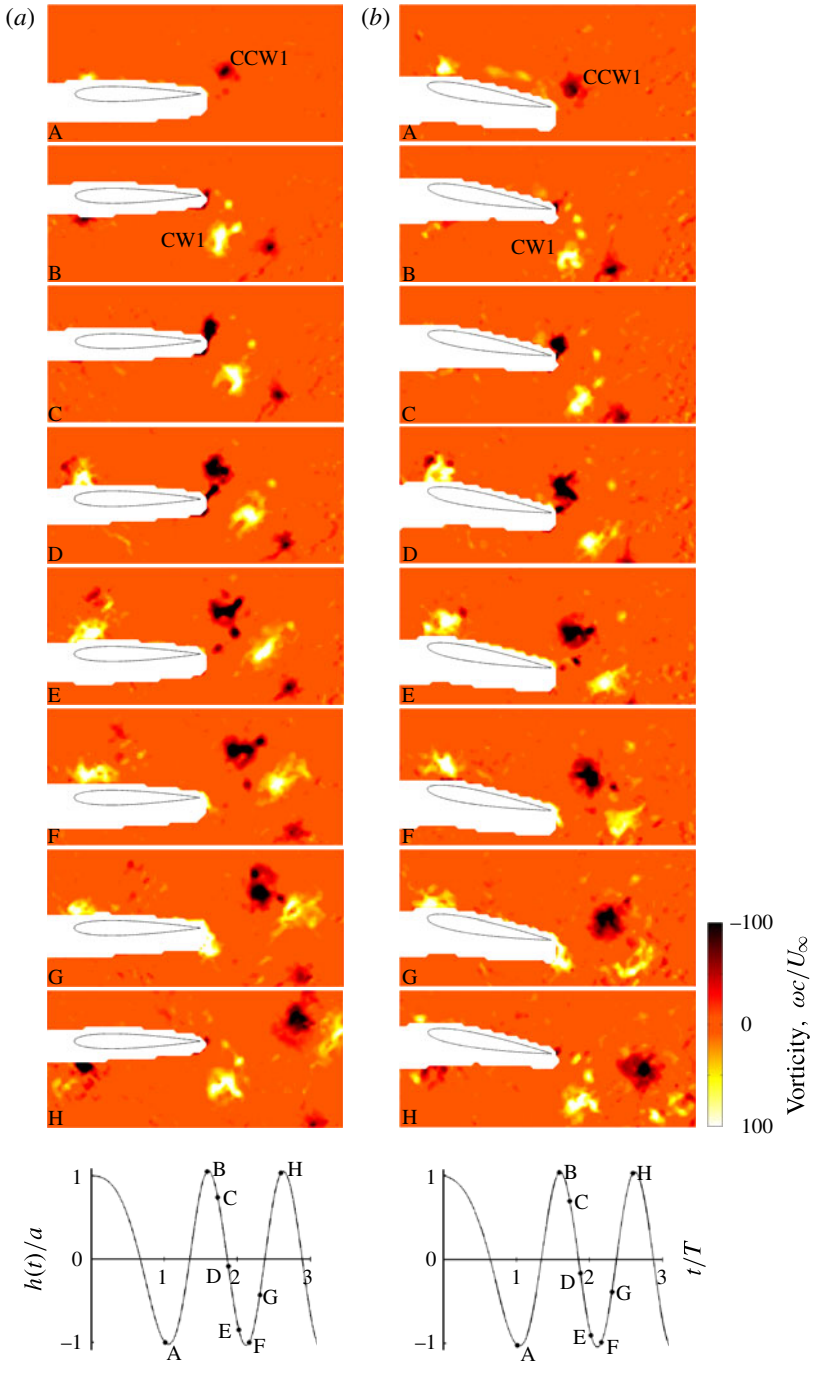

FIGURE 7. (Colour online) Normalized vorticity demonstrating the instantaneous starting flow for $a/c = 0.15$, $St_c = 2.025$, $h_i = a$, and (*a*) $\alpha = 0°$, (*b*) $\alpha = 10°$. Note the stronger first counter-clockwise vortex (CCW1) in the $\alpha = 10°$ case. This pairs with the first clockwise vortex, drawing it downwards and thereby creating a downward deflected jet.

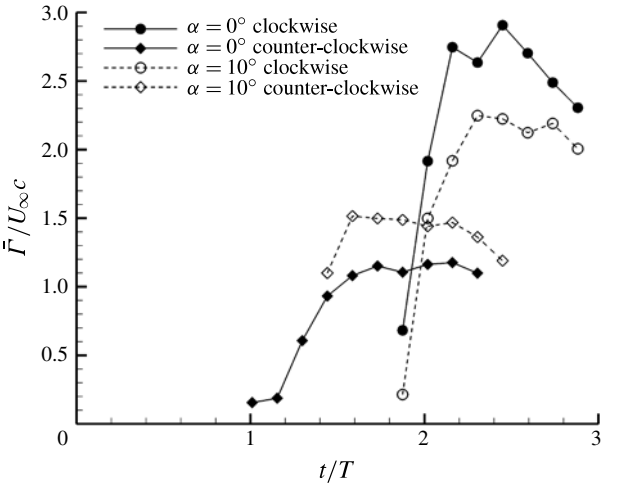

FIGURE 8. Normalized circulation of the first two trailing-edge vortices formed during the starting process from $h_i = a$, for $\alpha = 0°$ and $\alpha = 10°$.

and 2.00 for $a/c = 0.20$, 0.15 and 0.10 respectively; and for $\alpha = 10°$ are $St_c = 1.30$, 1.58 and 2.10 for $a/c = 0.20$, 0.15 and 0.10 respectively. These points are, however, approximate as how to define the bifurcation point is subjective and therefore accurate to one measurement interval. For $\alpha = 15°$ across all amplitudes there is no significant bifurcation. There is some minor hysteresis at the higher Strouhal numbers as previously described for $a/c = 0.15$ but this behaviour is not indicative of dual flows.

The time-averaged drag coefficient for the same cases as in figure 9 is shown in figure 10. For $\alpha = 0°$ (figure 10*a*), generally there is decreasing drag coefficient with increasing Strouhal number, with greater effect for greater amplitude as predicted by Garrick approximations and previously observed (Platzer *et al.* 2008). For this angle of attack for all amplitudes all three curves (increasing and decreasing frequency) match to within the bounds of experimental uncertainty across the entire Strouhal-number range. Hence, there is no sign of the bifurcation behaviour observed in the associated lift coefficient (figure 9*a*). This is a consequence of the symmetry at $\alpha = 0°$ which means that in terms of horizontal force there is no difference between upwards/downwards deflected jets because they are mirror images of each other in the horizontal plane and therefore create the same horizontal force component. With the angle of attack increased to $\alpha = 5°$ this symmetry is broken and a bifurcation is therefore observed, see figure 10(*b*). As observed in the lift coefficient, this only occurs for $a/c \geqslant 0.10$, and is amplitude dependent with the onset being at the same Strouhal numbers as observed in the lift coefficient. As a result of the bifurcation, the decreasing frequency case (downwards deflected jet) consistently produces more thrust. The magnitude of this difference in drag is small in comparison with that observed in the lift coefficient, i.e. $\Delta c_d \approx 0.5$ versus $\Delta c_l \approx 7.0$. Increasing the angle of attack to $\alpha = 10°$ amplifies this difference, $\Delta c_d \approx 0.75$. The onset of bifurcation is again amplitude dependent reflecting the points observed in the lift coefficient. With the angle of attack increased to $\alpha = 15°$ (figure 10*d*), there is no longer a bifurcation at any amplitude, again reflecting the trends observed in lift coefficient.

From complementary phase-averaged PIV measurements, the angle of the deflected jet was measured by tracking the motion of the trailing-edge vortices. Figure 11(*a*) for

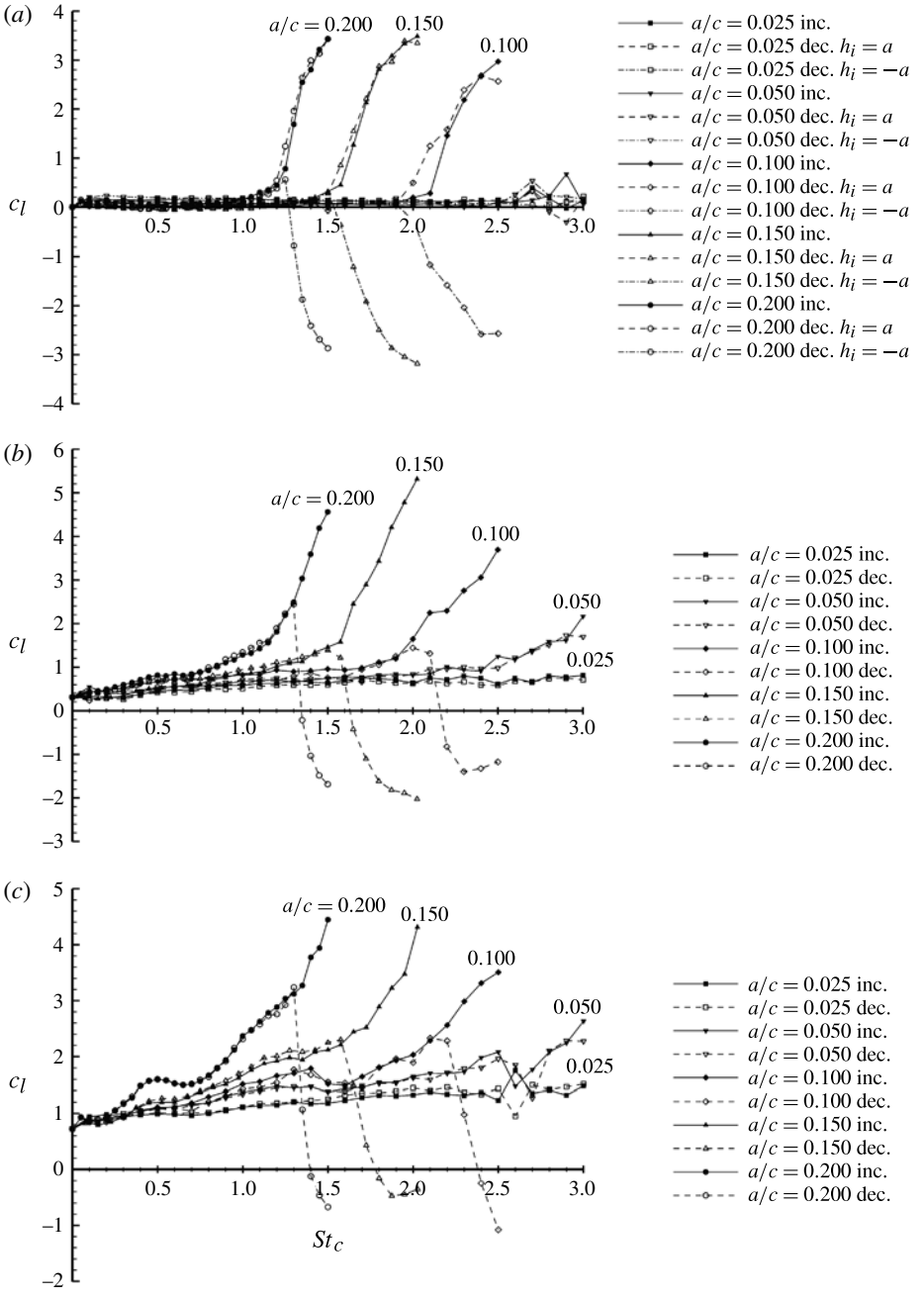

FIGURE 9. For caption see next page.

$\alpha = 0°$ reaffirms that in the pre-bifurcation regime the vortices convect approximately horizontally. After bifurcation, for mode A, the vortex trajectory angle becomes negative, indicative of an upwards deflected jet; for mode B the vortex trajectory angle becomes positive, indicative of a downward deflected jet. Figure 11(*b,c*) confirms similar trends for $\alpha = 5°$ and $\alpha = 10°$ but with a bias towards positive vortex trajectory angles due to the non-zero angle of attack.

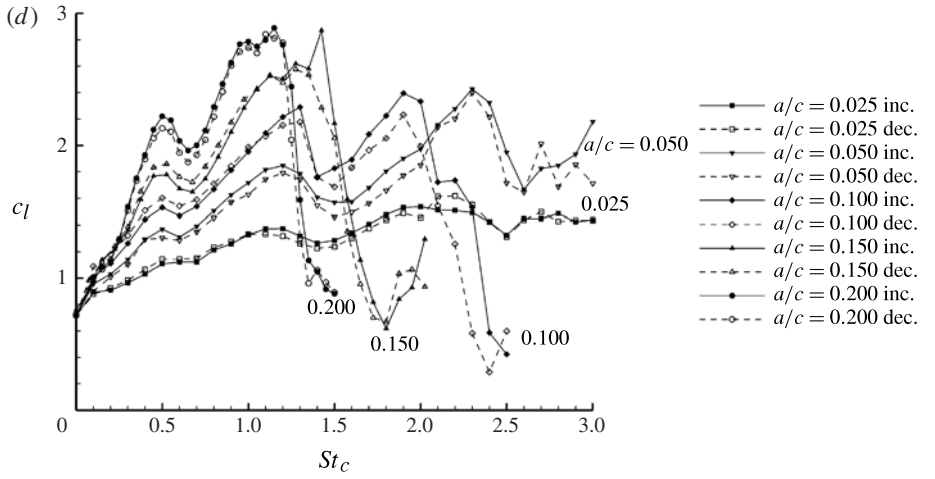

FIGURE 9. (cntd). Lift coefficient as a function of St_c for: (*a*) $\alpha = 0°$; (*b*) $\alpha = 5°$; (*c*) $\alpha = 10°$; (*d*) $\alpha = 15°$. Increasing frequency: solid lines and full symbols; decreasing frequency: dashed lines and open symbols. Unless stated in the legend the starting position for decreasing frequency is $h_i = 0$ ($(t/T)_s = 0.25$).

3.6. *Bifurcation criteria*

In this section several criteria to predict the onset of bifurcation will be introduced. To this end shown in figure 12 are the points of bifurcation in the amplitude–Strouhal number domain. Also shown is a power-law curve fit of the drag to thrust switch points as derived from figure 10. These show that the location of the switch from drag to thrust is highly amplitude dependent with earlier zero drag for greater amplitude. The point of zero drag is also delayed by increasing angle of attack due to the increased drag of the stationary aerofoil. The single–dual flow field boundary is likewise delayed to higher Strouhal numbers by increasing angle of attack but the effect is not as pronounced. Extrapolation of these curves to smaller amplitudes and higher Strouhal numbers shows that dual flow was not observed at the smaller amplitudes ($a/c = 0.025$ and $a/c = 0.05$) because the maximum Strouhal number studied was insufficient.

The trend of increasing Strouhal number with decreasing amplitude suggests the possibility of a constant plunge velocity or effective angle of attack as criteria for the onset of bifurcation. Figure 13 therefore shows the bifurcation onset points as symbols plotted against both Strouhal number based on amplitude and effective angle of attack. Effective angle of attack varies in a range so the limits of this range ($\alpha_{eff,min}$ and $\alpha_{eff,max}$) are used in figure 13. The points representing the onset of bifurcation fall within the range $St_A = 0.45 \pm 0.07$ which is in very close agreement with the range $0.434 < St_A < 0.455$ suggested by von Ellenrieder & Pothos (2008). The trend of decreasing St_A with decreasing amplitude and angle of attack means however that this cannot be considered a universal criterion. In terms of effective angle of attack the points fall within the range $\alpha_{eff,max} = 60° \pm 9°$; however again due to the trend of decreasing effective angle of attack with amplitude and angle of attack this cannot be considered a universal criterion. In addition, neither plunge velocity nor effective angle of attack gives an adequate explanation for why there is no bifurcation at larger angles of attack ($\alpha > 10°$).

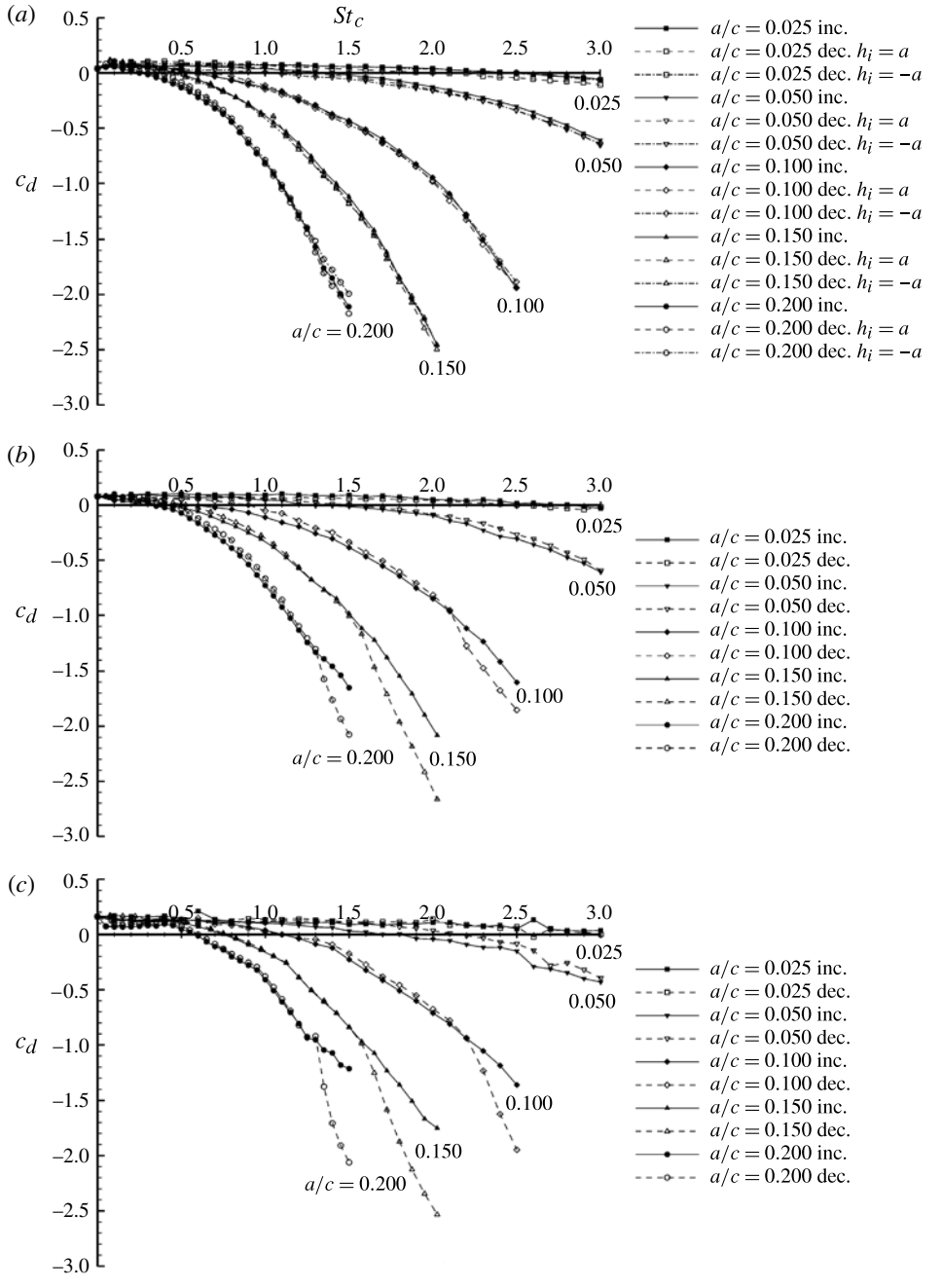

FIGURE 10. For caption see next page.

As a simple universal criterion cannot be defined from the controllable experimental parameters it is necessary instead to derive a criterion from the flow field measurements. All phase-averaged flow data are taken after the flow has settled, following a change in frequency. The bifurcation criteria are therefore for the stable branches. For this, we will focus on the trailing-edge vortex properties for the reasons explained below.

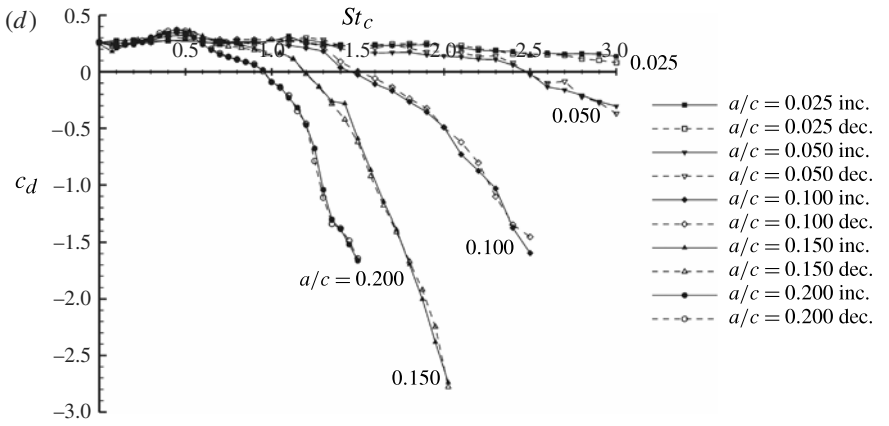

FIGURE 10. (cntd). Drag coefficient as a function of St_c for: (*a*) $\alpha = 0°$; (*b*) $\alpha = 5°$; (*c*) $\alpha = 10°$; (*d*) $\alpha = 15°$. Increasing frequency: solid lines and full symbols; decreasing frequency: dashed lines and open symbols. Unless stated in the legend the starting position for decreasing frequency is $h_i = 0$ ($(t/T)_s = 0.25$).

At the high Strouhal numbers typical of the bifurcation flow field the leading-edge vortex is formed during the downward motion but impinges on the aerofoil during its upward motion, resulting in the loss of the coherency of the vortex. This strong interaction disintegrates the leading-edge vortex (Cleaver *et al.* 2011). It is therefore not convected into the wake (see figures 5 and 7) and so does not interact with the trailing-edge vortices. This would suggest that the trailing-edge vortices alone are responsible for deflected jets and any criteria should be derived from their properties. This is supported by the results of Jones *et al.* (1998), who simulated deflected jets with an inviscid unsteady panel code, where no leading-edge vortex exists as separation is not modelled. The model proposed by Godoy-Diana *et al.* (2009) used the measured strength of the trailing-edge vortices and the phase velocity of the vortex street. However, it did not accurately predict deflected jets for our data. It is not known whether this is due to the plunging motion used in this study rather than the pitching motion used by Godoy-Diana *et al.* (2009).

Shown in figure 14 is the circulation of the TEVs for $\alpha = 0°$, 5°, 10° and 15°, for $a/c = 0.05$, 0.10, 0.15 and 0.20. Clockwise TEVs are denoted by solid lines and counter-clockwise TEVs by dashed lines. The pre-bifurcation case is denoted by solid symbols, with mode A treated as a continuation of this, and mode B denoted by open symbols. For $\alpha = 0°$ both trailing-edge vortices grow almost identically with increasing Strouhal number until the point of bifurcation. After the point of bifurcation the asymmetric wake creates asymmetry in the strengths of the clockwise and counter-clockwise vortices. For mode A the clockwise vortex becomes stronger than the counter-clockwise vortex, and vice-versa for mode B. There is a strong amplitude dependence of the trailing-edge vortex strength. For $\alpha = 5°$ the same basic trend is observed except that the clockwise circulation curve is shifted downwards and the counter-clockwise curve is shifted upwards. This is due to the greater mean angle of attack causing greater asymmetry in the effective angle of attack as demonstrated in figure 13. The circulation gap between clockwise and counter-clockwise vortices is further enhanced by $\alpha = 10°$.

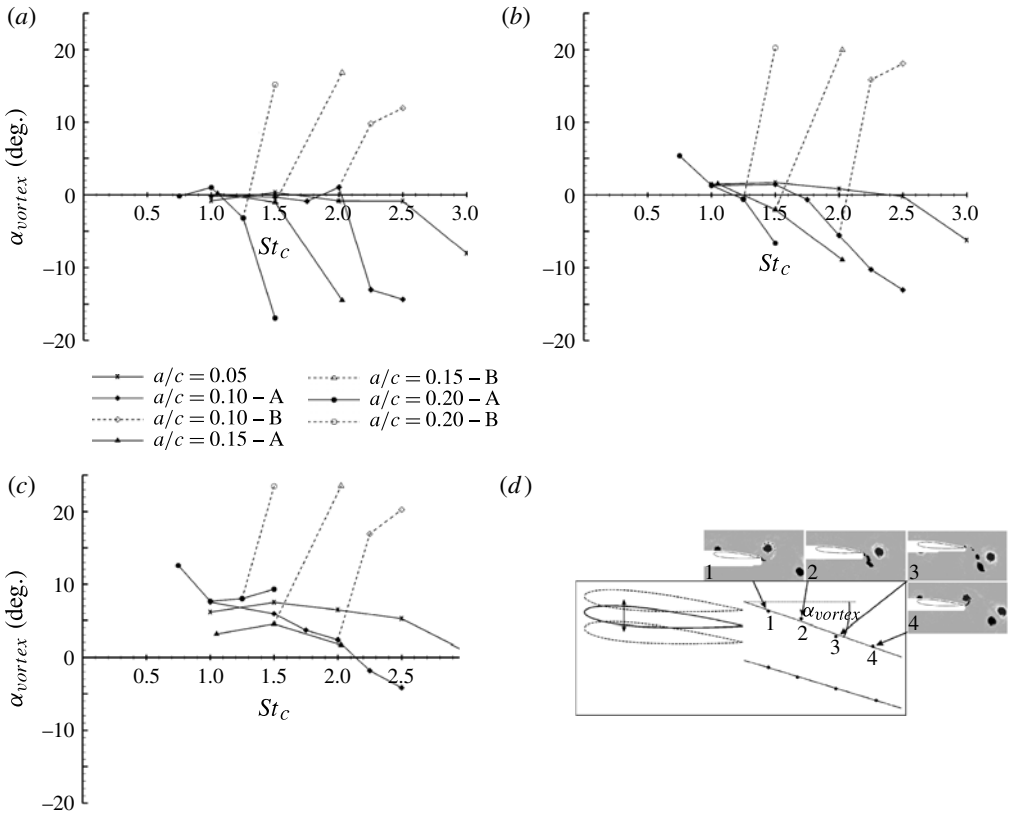

FIGURE 11. Trailing-edge-vortex trajectory angle for: (*a*) $\alpha = 0°$; (*b*) $\alpha = 5°$; (*c*) $\alpha = 10°$; and (*d*) method used to determine α_{vortex} for the counter-clockwise TEV. It is first located in the phase-averaged data, a line of best fit is then applied giving a gradient related to α_{vortex}. The sign convention for α_{vortex} is positive for a downwards deflected jet, and negative for an upwards deflected jet.

For $\alpha = 15°$ this trend of increased counter-clockwise vortex circulation and reduced clockwise trailing-edge vortex circulation is continued, however now only a single mode is observed, one with a stronger counter-clockwise vortex than clockwise vortex. The circulation measurements for the smaller angles of attack demonstrate that this is typical of a mode B flow field. Indeed when comparing the flow field for $\alpha = 15°$ with the mode B flow field for $\alpha = 5°$ and $\alpha = 10°$ (see figure 15), it bears all the hallmarks of a mode B flow field and yet without a point of bifurcation it is not possible to classify it as such. In summary, the increasing angle of attack causes greater asymmetry in the effective angle of attack which causes an imbalance in the trailing-edge vortex strengths, inclining the wake towards a downward deflected jet. To characterize this asymmetry a new parameter is suggested based on the angular velocity of a vortex pair (Milne-Thomson 1968):

$$\frac{(\Gamma_{T+} + \Gamma_{T-})}{d^2} \tag{3.4}$$

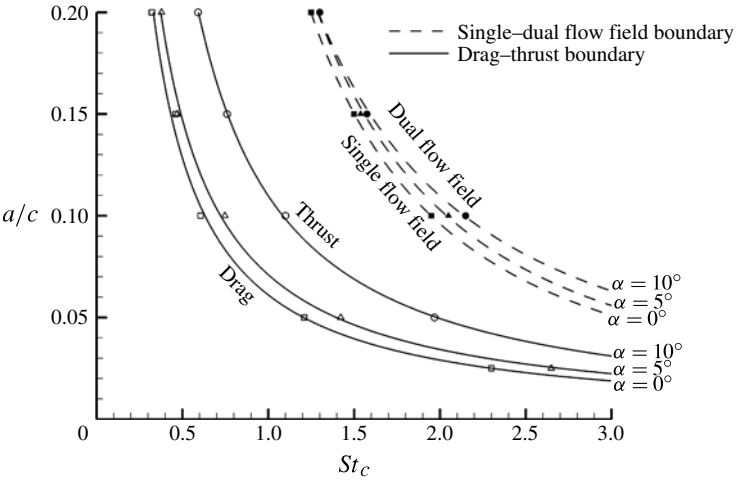

FIGURE 12. Boundary between drag/thrust producing and single/dual flow field for: $\alpha = 0°$ (square); $\alpha = 5°$ (triangle); and $\alpha = 10°$ (circle). Lines are power-law curve fits.

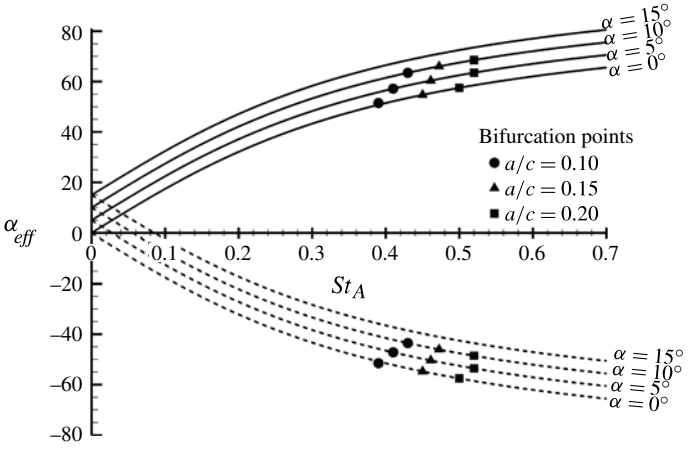

FIGURE 13. Effective angle of attack as a function of Strouhal number based on amplitude. Solid line: $\alpha_{eff,max}$, dashed line: $\alpha_{eff,min}$. Symbols denote the point of bifurcation as determined from the force measurements.

where d is the distance between the vortices. This is made dimensionless as

$$\frac{(\Gamma_{T+} + \Gamma_{T-})c}{U_\infty d^2}. \tag{3.5}$$

This represents a non-dimensional trailing-edge vortex *asymmetry parameter*. Our data suggest that the mode-A flow field is not possible once this asymmetry parameter exceeds a critical value, as will be discussed further.

In a similar manner, it is possible to consider the minimum plunge velocity criteria in terms of the experimentally measured circulation. Shown in figure 16 is the average absolute circulation of the two trailing-edge vortices versus Strouhal number. The average circulation is used so as to minimize and separate out any asymmetry effects.

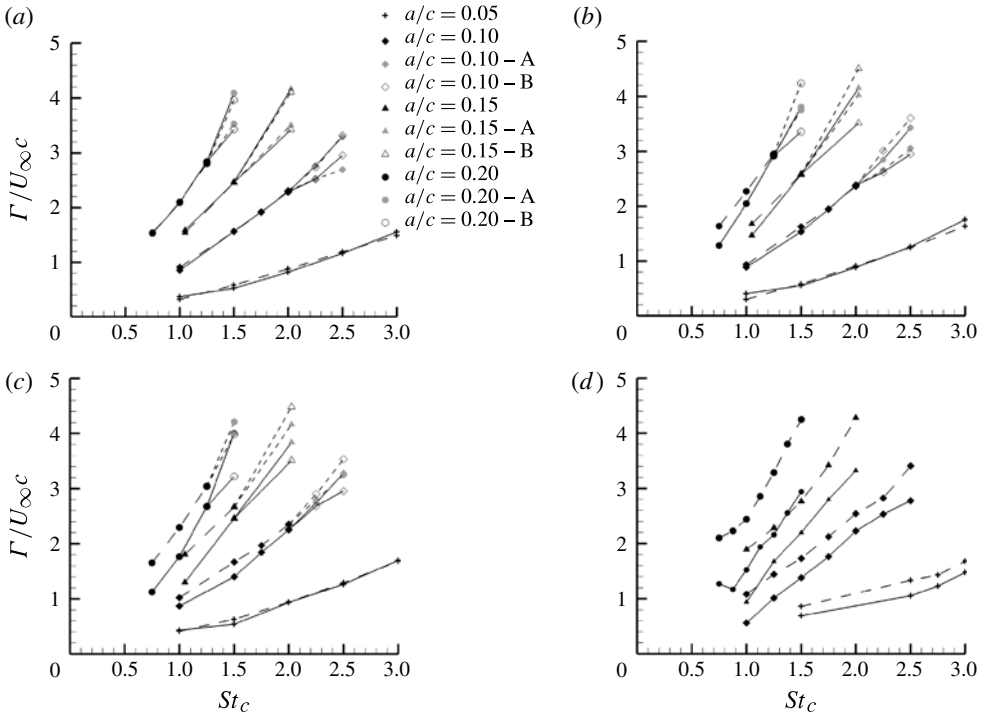

FIGURE 14. Absolute circulation for: (*a*) $\alpha = 0°$; (*b*) $\alpha = 5°$; (*c*) $\alpha = 10°$; (*d*) $\alpha = 15°$. Solid line represents the clockwise TEV, and dashed line the counter-clockwise TEV.

For the different angles of attack the curves collapse onto a nearly parabolic trend with the gradient determined by the amplitude. The points of bifurcation are identified through the dashed line. This shows that a minimum threshold trailing-edge-vortex circulation is required for bifurcation to occur. The trend with amplitude suggests that bifurcation requires larger trailing-edge-vortex circulation at larger amplitudes. This is rational since larger amplitude leads to larger trailing-edge-vortex spacing which inhibits vortex pairing. If this trend is extrapolated to higher St_c, it is clear that for $a/c = 0.05$ the level of trailing-edge-vortex circulation is insufficient for bifurcation (within the Strouhal-number range tested).

Combining both the asymmetry parameter and the normalized circulation parameter produces figure 17. A horizontal boundary separating the single and dual modes is shown; and a vertical boundary separating mode A and mode B is revealed. The question of why there is no bifurcation at low amplitudes is therefore answered by the circulation threshold, and the question of why there is no mode A at large angles of attack is answered by the asymmetry boundary, i.e. all the points for $\alpha = 15°$ lie to the mode B side of the boundary.

The threshold circulation displayed in figure 17 is however not perfect, as seen by the scatter. As the aerofoil is in effect acting as a vortex generator with the strength determined by the plunge velocity, plunge velocity is a more logical normalizing variable. Shown in figure 18 is this alternative circulation parameter with the same asymmetry parameter. As expected the data points have collapsed down to a smaller band, but more importantly there is now a clear boundary between the single and dual

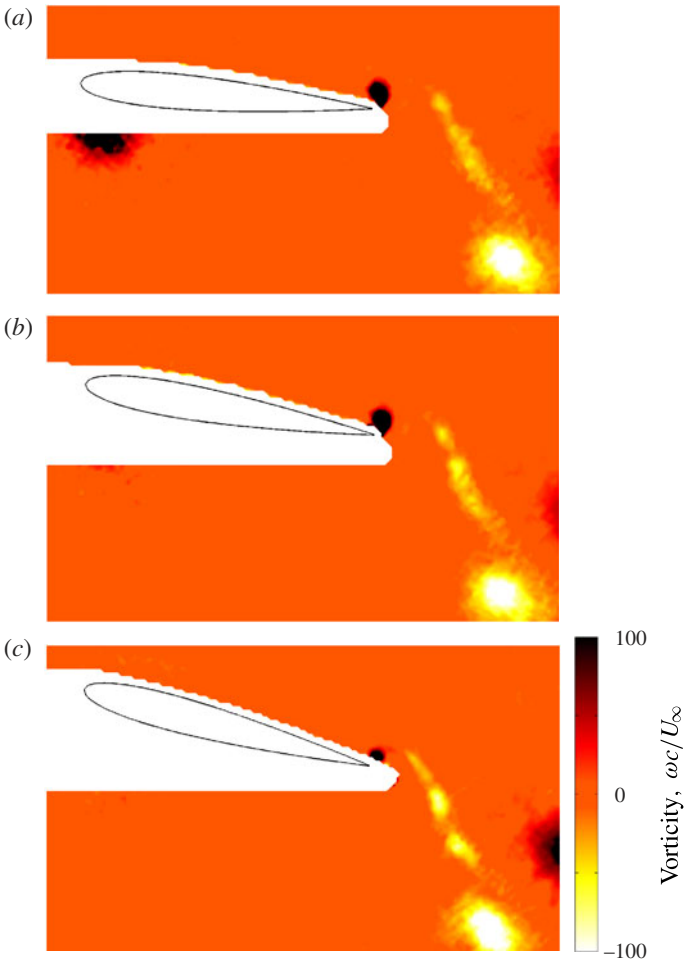

FIGURE 15. (Colour online) Vorticity contours showing the similarity of flow fields across different angles of attack for $a/c = 0.150$, $St_c = 2.025$ and: (*a*) $\alpha = 5°$ – mode B; (*b*) $\alpha = 10°$ – mode B; and (*c*) $\alpha = 15°$.

modes with minimal scatter of the data. The critical value of circulation normalized by plunge velocity corresponding to the bifurcation points is $\bar{\Gamma}/U_P c = 1.85$.

Alternatively, figure 19 shows all the trailing-edge-vortex circulations for all amplitudes and angles of attack plotted against St_A. This figure demonstrates the three possible bifurcation criteria: $St_A = 0.45 \pm 0.07$ on the x-axis, $\bar{\Gamma}/U_\infty c = 2.65 \pm 0.45$ on the y-axis, and $\bar{\Gamma}/U_P c = 1.85$ as a straight line with its gradient determined by

$$\frac{\bar{\Gamma}}{U_P c} = \frac{\bar{\Gamma}}{\pi U_\infty St_A c} = 1.85; \tag{3.6}$$

therefore,

$$\frac{\bar{\Gamma}}{U_\infty c} = 1.85\pi St_A. \tag{3.7}$$

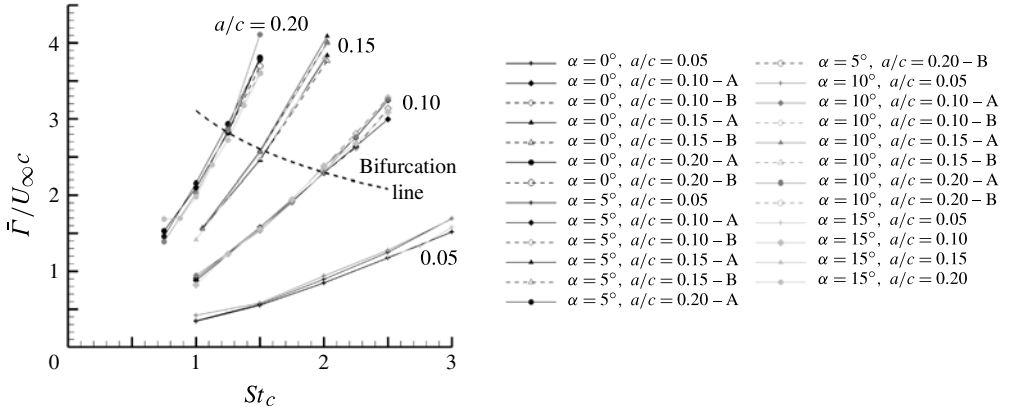

FIGURE 16. Average absolute TEV circulation as a function of Strouhal number.

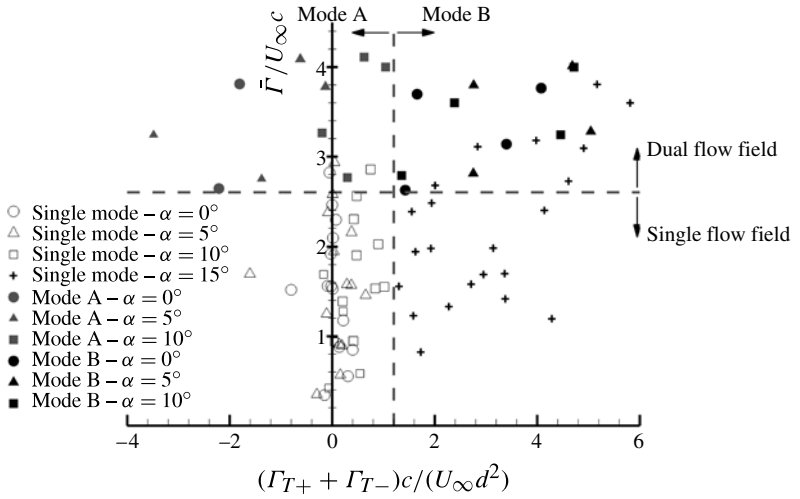

FIGURE 17. Normalized circulation as a function of asymmetry parameter.

This line passes through the points of bifurcation with the values above being dual mode and the values below single mode. Hence, this reinforces the significance of plunge velocity in determining the trailing-edge vortex strength. The circulation normalized by the plunge velocity, $\Gamma/U_P c = \Gamma/(2\pi fac)$, can be also interpreted as the inverse of a modified Strouhal number based on the dipole velocity Γ/a, the frequency and chord length.

4. Conclusions

Time-averaged force measurements on a periodically plunging NACA 0012 aerofoil have identified significant bifurcations at high Strouhal numbers for angles of attack smaller than and equal to the stall angle. These bifurcations were observed when the frequency of the oscillations was increased slowly up to a maximum value and the motion was stopped, and then restarted impulsively at the maximum frequency and

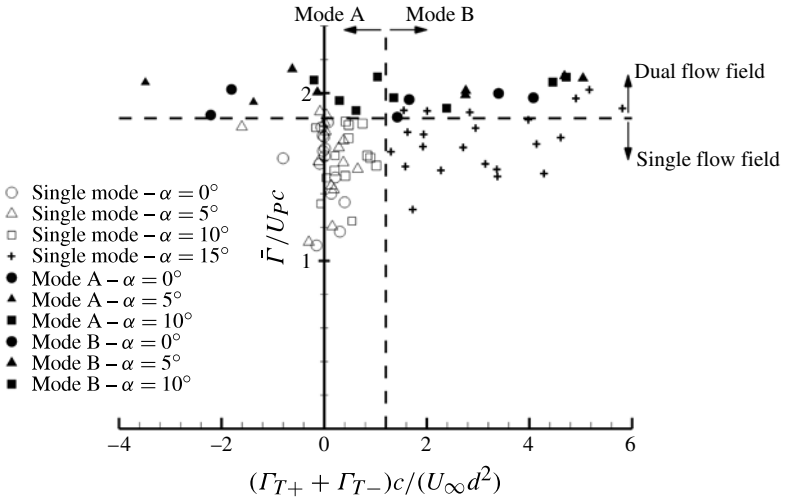

FIGURE 18. Circulation normalized by plunge velocity as a function of asymmetry parameter.

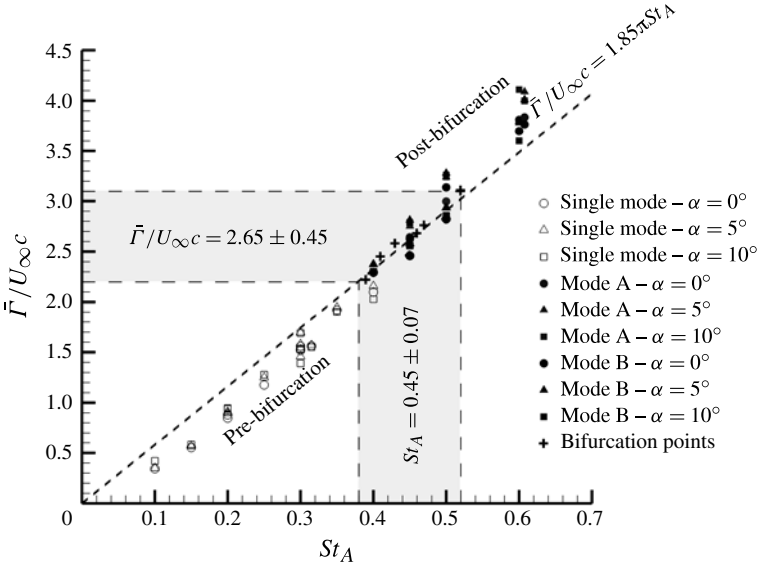

FIGURE 19. TEV normalized circulation as a function of Strouhal number based on amplitude. Crosses denote onset of bifurcations. Dashed line of gradient 1.85π represents the bifurcation constant derived from figure 18.

the frequency was decreased very slowly. Each time the frequency was changed, we waited for sufficient time for the flow to reach an asymptotic state before recording data. It was found that below a critical frequency, lift force and flow fields were identical; however, above this bifurcation frequency, dual flows and significantly different lift forces were observed. These dual flows were characterized as thrust-producing deflected jets. These are produced by the trailing-edge vortex loitering over

the aerofoil to form a vortex dipole with the opposite-sign vortex. This behaviour also modifies the leading-edge vortices and may produce very high lift coefficients. The lift direction is the same as the direction of the vertical component of the deflected jet. The direction of these deflected jets is determined by the initial conditions and the angle of attack. Following an impulsive start, a stable flow is established in approximately two plunging cycles.

Effective angle of attack due to the plunging motion or the Strouhal number based on amplitude has some correlation with the onset of bifurcation. However, better correlations and insight into the flow physics were derived from the flow field measurements. Analysis of the trailing-edge vortices lead to two parameters which describe the wake behaviour. First, an asymmetry parameter is derived from the difference in circulation of the clockwise and counter-clockwise trailing-edge vortices. This parameter determines whether the deflected jet is deflected upwards or downwards. It also explains why dual flows are not observed at larger angles of attack as the greater asymmetry in the effective angle of attack causes an imbalance in the trailing-edge-vortex strengths, which gives a natural tendency towards a downwards deflected jet. Secondly, a strength parameter is derived from the average of the circulations of the trailing-edge vortices. From the measured values of circulation, this parameter can be expressed as circulation normalized by the free-stream velocity or circulation normalized by the plunge velocity. It was shown that a minimum value of the strength parameter is necessary for bifurcation to occur. The bifurcation was therefore not observed at small amplitudes or low frequencies, due to insufficient trailing-edge-vortex strength. Circulation normalized by the plunge velocity gives the best data collapse, and can be interpreted as the inverse of a modified Strouhal number based on the dipole velocity.

Acknowledgements

This work was sponsored by the Air Force Office of Scientific Research, Air Force Material Command, USAF under grant number FA8655-10-1-3093, monitored by Dr D. Smith, as well as the Engineering and Physical Sciences Research Council (EPSRC) Studentship, and the RCUK Academic Fellowship in Unmanned Air Vehicles.

REFERENCES

BOHL, D. G. & KOOCHESFAHANI, M. M. 2009 MTV measurements of the vortical field in the wake of an airfoil oscillating at high reduced frequency. *J. Fluid Mech.* **620**, 63–88.

BRATT, J. B. 1950 Flow patterns in the wake of an oscillating airfoil. *Aero. Res. Counc. R&M* 2773.

CLEAVER, D. J., WANG, Z. J. & GURSUL, I. 2009*a* Delay of stall by small amplitude airfoil oscillation at low Reynolds numbers. *AIAA Paper* 2009-392.

CLEAVER, D. J., WANG, Z. J. & GURSUL, I. 2009*b* Lift enhancement on oscillating airfoils. *AIAA Paper* 2009-4028.

CLEAVER, D. J., WANG, Z. & GURSUL, I. 2010 Vortex mode bifurcation and lift force of a plunging airfoil at low Reynolds numbers. *AIAA Paper* 2010-390.

CLEAVER, D. J., WANG, Z. & GURSUL, I. 2011 Lift enhancement by means of small amplitude airfoil oscillations at low Reynolds numbers. *AIAA J.* **49** (9), 2018–2033.

VON ELLENRIEDER, K. D. & POTHOS, S. 2008 PIV measurements of the asymmetric wake of a two-dimensional heaving hydrofoil. *Exp. Fluids* **44** (5), 733–745.

EMBLEMSVAG, J. E., SUZUKI, R. & CANDLER, G. 2002 Numerical simulation of flapping micro air vehicles. *AIAA Paper* 2002-3197.

FRAMPTON, K. D., GOLDFARB, M., MONOPOLI, D. & CVETICANIN, D. 2002 Passive aeroelastic tailoring for optimal flapping wings. In *Fixed and Flapping Wing Aerodynamics for Micro Air Vehicle Applications* (ed. T. J. Mueller), pp. 473–482. AIAA.

GODOY-DIANA, R., AIDER, J. L. & WESFREID, J. E. 2008 Transitions in the wake of a flapping foil. *Phys. Rev.* E **77**, 1.

GODOY-DIANA, R., MARAIS, C., AIDER, J. L. & WESFREID, J. E. 2009 A model for the symmetry breaking of the reverse Benard–von Kármán vortex street produced by a flapping foil. *J. Fluid Mech.* **622**, 23–32.

GRAFTIEAUX, L., MICHARD, M. & GROSJEAN, N. 2001 Combining PIV, POD and vortex identification algorithms for the study of unsteady turbulent swirling flows. *Meas. Sci. Technol.* **12** (9), 1422–1429.

HEATHCOTE, S. & GURSUL, I. 2007*a* Flexible flapping airfoil propulsion at low Reynolds numbers. *AIAA J.* **45** (5), 1066–1079.

HEATHCOTE, S. & GURSUL, I. 2007*b* Jet switching phenomenon for a periodically plunging airfoil. *Phys. Fluids* **19**, 2.

HO, S., NASSEF, H., PORNSINSIRIRAK, N., TAI, Y. C. & HO, C. M. 2003 Unsteady aerodynamics and flow control for flapping wing flyers. *Prog. Aerosp. Sci.* **39** (8), 635–681.

JONES, K. D., DOHRING, C. M. & PLATZER, M. F. 1998 Experimental and computational investigation of the Knoller–Betz effect. *AIAA J.* **36** (7), 1240–1246.

LEWIN, G. C. & HAJ-HARIRI, H. 2003 Modelling thrust generation of a two-dimensional heaving airfoil in a viscous flow. *J. Fluid Mech.* **492**, 339–362.

LIANG, C. L., OU, K., PREMASUTHAN, S., JAMESON, A. & WANG, Z. J. 2011 High-order accurate simulations of unsteady flow past plunging and pitching airfoils. *Comput. Fluids* **40** (1), 236–248.

MILNE-THOMSON, L. M. 1968 *Theoretical Hydrodynamics*. Macmillan.

MOFFAT, R. J. 1988 Describing the uncertainties in experimental results. *Exp. Therm. Fluid Sci.* **1** (1), 3–17.

MORGAN, C. E., BABINSKY, H. & HARVEY, J. K. 2009 Vortex detection methods for use with PIV and CFD data. *AIAA Paper* 2009-74.

PLATZER, M. F., JONES, K. D., YOUNG, J. & LAI, J. C. S. 2008 Flapping-wing aerodynamics: progress and challenges. *AIAA J.* **46** (9), 2136–2149.

SANE, S. P. 2003 The aerodynamics of insect flight. *J. Expl Biol.* **206** (23), 4191–4208.

SHYY, W., BERG, M. & LJUNGQVIST, D. 1999 Flapping and flexible wings for biological and micro air vehicles. *Prog. Aerosp. Sci.* **35** (5), 455–505.

TRIANTAFYLLOU, M. S., TRIANTAFYLLOU, G. S. & YUE, D. K. P. 2000 Hydrodynamics of fishlike swimming. *Annu. Rev. Fluid Mech.* **32**, 33–53.

VISBAL, M. R. 2009 High-fidelity simulation of transitional flows past a plunging airfoil. *AIAA J.* **47** (11), 2685–2697.

WANG, Z. J. 2000 Two-dimensional mechanism for insect hovering. *Phys. Rev. Lett.* **85** (10), 2216–2219.